An Underactuated Cable-Driven Parallel Robot for Marine Automated Launch and Recovery Operations

An Underactuated Cable-Driven Parallel Robot for Marine Automated Launch and Recovery Operations*

Michele Angelini‡
Edoardo Ida'†‡
Dept. of Industrial Engineering
University of Bologna
Bologna 40138, Italy
Email addresses:
michele.angelini2@unibo.it
edoardo.ida2@unibo.it

Daniele Bertin‡
Enrico Mantovani
Davide Bazzi
Vincenzo Orassi
L3Harris
Milano 20142, Italy
and Bologna 40012, Italy
Email addresses:
daniele.bertin@l3harris.com
enrico.mantovani@l3harris.com
davide.bazzi@l3harris.com
vincenzo.orassi@l3harris.com

Marco Carricato
Dept. of Industrial Engineering
University of Bologna
Bologna 40138, Italy
Email: marco.carricato@unibo.it

This paper presents the feasibility study and preliminary testing of an underactuated cable-driven parallel robot for automated launch *and* recovery *operations on the sea surface. The robot frame is mounted onto a primary vessel (*PV*) subject to sea-induced motions. During* launch*, the end-effector (*EE*) is required to deploy a secondary vessel (*SV*) by lowering it from the* PV *onto the sea surface. During* recovery*, the* EE *has to track and grasp a* SV *and the* EE-SV *assembly needs to be stabilized during lifting from the sea surface to the* PV*. Sea conditions and the underactuated nature of the* EE *influence the operational feasibility and the overall robot performance. The paper presents the conceptual design and the robot model, as well as the methodologies for winch dimensioning and robot control. An extensive simulation campaign is conducted to optimize performances and assess the system behavior. Finally, the operations are tested on a scaled prototype in a laboratory environment.*

NOMENCLATURE

Abbreviations

CDPR	Cable-Driven Parallel Robot
EE	End-Effector
DoFs	Degrees of Freedom
PV	Primary Vessel
SV	Secondary Vessel
ALARS	Automatic Launch and Recovery System

Geometric symbols

$\mathbf{p}, \mathbf{p}_B, \mathbf{p}_L$	*EE*, *PV*, and *SV* position
$\boldsymbol{\epsilon}, \boldsymbol{\theta}_B, \boldsymbol{\theta}_L$	*EE*, *PV*, and *SV* orientation
$\boldsymbol{\zeta}, \boldsymbol{\zeta}_B$	*EE*, and *PV* pose
$\mathbf{d}$	Displacement of the *SV* from the *EE*

*A preliminary version of this paper was accepted for presentation at the ASME IDETC-CIE 2023, to be held in Boston, MA, USA, on August 20-23 2023 [1]

†Address all correspondence for other issues to this author.

‡Joint first authors.

Kinematic symbols

$\boldsymbol{\omega}$, $\boldsymbol{\omega}_B$, $\boldsymbol{\omega}_L$	*EE*, *PV*, and *SV* angular velocity
$\mathbf{v}$, $\mathbf{v}_B$	*EE*, and *PV* twist
$\boldsymbol{\alpha}_L$	*SV* angular acceleration
$\boldsymbol{\Xi}$	kinematic Jacobian

Dynamic symbols

$\mathbf{s}$	position of the *EE* center of mass G
$\mathbf{s}_L$	position of the *SV* center of mass G_L
$\mathbf{I}_P$, $\mathbf{I}_L$	*EE*, and *SV* inertia tensors about P
$\mathbf{M}$	*EE* Mass matrix
m, m_L	*EE*, and *SV* mass
$\mathbf{C}$	*EE* Coriolis matrix
$\boldsymbol{\tau}$	cable-tension array

1 INTRODUCTION

Cable-driven parallel robots (*CDPRs*) control the motion of an end-effector (*EE*) thanks to extendable cables connected in a parallel fashion to it. *CDPRs* act as high-speed, collaborative cranes and the flexibility of these robotic devices recently attracted a lot of attention in the industry: entertainment [2], logistics [3], construction [4], maintenance [5] and inspection [6] are just a few of the studied applications. Introducing these systems to supplement or replace standard hoisting devices in off-shore environments has also shown a rising tendency since *CDPRs* may operate autonomously and self-regulate thanks to feedback control. *CDPRs* may allow sea-surface operations to be faster and safer, as standard cranes alone cannot compensate for payload swinging due to wave-induced disturbances or wind gusts [7]. On the other hand, the main problem affecting cable-driven systems is that cables can only exert pulling forces and wave-induced frame oscillations may lead to cable slackness. To preserve the system safety and performance, appropriate controllers must be designed to avoid tension loss [8].

One of the first practical applications of *CDPRs* for off-shore activities was approached in [9], where the ship oscillatory behaviors were forecast with neural networks and a 6-cable system compensated the payload swinging. Later, mitigation of waves effects was addressed by employing overconstrained CDPRs, equipped with more cables than the *EE* degrees of freedom (*DoFs*): robot control models were adapted to account for cable slackness [10, 11] and, additionally, tension distribution strategies were developed to eliminate slackness [12]. Undoubtedly, using overconstrained systems may be advantageous in precision applications since the *EE* controllability is the highest possible. Nevertheless, many cables heavily weigh on workspace accessibility, production costs and maintenance complexity. In an off-shore context, reliability and simplicity are of the utmost importance: salt mist and seawater lead to high rates of equipment deterioration and out-of-port interventions are not always possible. To this end, simpler systems requiring six or fewer cables have been studied and specifically tailored for this kind of application [13, 14].

This paper introduces the development of an underactuated cable-driven parallel robot to be mounted on a primary vessel (*PV*) and used as a crane-aiding device for off-shore handling operations, whose concept was introduced in the patent application [15]. In particular, its task-oriented control and dimensioning are addressed. The robot has to perform two specific tasks: deploying a secondary vessel (*SV*) from the *PV* to the water surface (*launch* operation) and recovering the *SV* from the water surface (*recovery* operation). Employing an underactuated system significantly increases workspace accessibility and limits machine complexity, but it does not allow to control every *DoF* of the *EE* [16, 17, 18]. To address this problem, the robot is intentionally designed to have an *EE* as close as practically possible to a point-mass [19] and two controllers are designed to fulfill the objectives of the handling operations. An extensive simulation campaign is conducted to concurrently (i) tune controllers' parameters and (ii) obtain system specifications in terms of the maximum required cable tension and power, which are the most critical design parameters [20]. Experiments on the robot operations are performed on a scaled prototype, in order to show the promising results of the application of this technology in a realistic scenario.

The structure of the paper is as follows. Section 2 describes the tasks to be performed, the system requirements and its conceptual design. Section 3 details the system model. Section 4 introduces the task-oriented controllers. Section 5 is dedicated to the simulation campaign, performance optimization and evaluation of the system limitations. Section 6 presents the experimental results in a laboratory set-up, and conclusions are drawn in Section 7. With respect to the preliminary conference version of this paper [1], Section 6 is completely new.

2 SYSTEM REQUIREMENTS AND CONCEPTUAL DESIGN

The system has to perform two tasks: *launch* and *recovery*. When a standard hoisting device, such as a lifting crane, is employed, the launch operation consists in lowering a *SV* from a *PV* to the sea surface; the *SV* is connected to the crane cable through a hook and it is

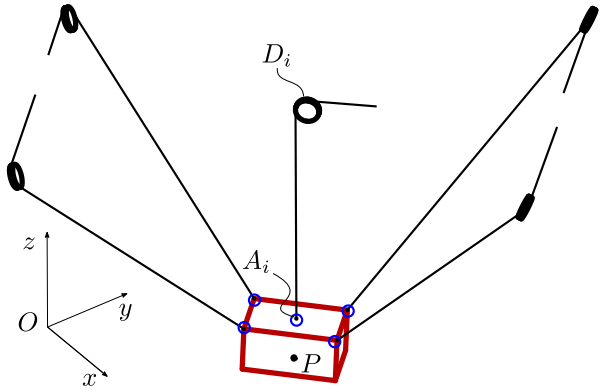

Fig. 1: Underactuated 4-cable parallel robot coupled with a central hoisting device.

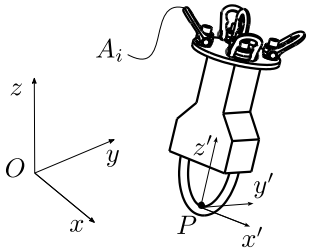

Fig. 2: Representation of the end-effector

slowly lowered until the cable slackens and an operator on the *SV* disengages it. While the *SV* is lowered, ship workers on the *PV* attempt to damp *SV* oscillations with additional ropes manually. The standard recovery of a *SV* from a *PV* starts with the deployment of the hook attached to the hoisting device, followed by the workers on the *SV* securing the hook on a grasping point. After the hook is connected, the *SV* can be lifted and its oscillations are manually damped, as in the launch operation. These tasks are thus (i) labor intensive and (ii) dangerous if sea conditions are even mild: the operators may not be able to manually damp *SV* oscillations, thus endangering vessels and workers.

The aim of a robotic, automatic *launch* and *recovery* system (*ALARS* in short) is to remove vessel personnel from danger and achieve autonomy. A robot dedicated to *launch* would be required to lower the *SV* to the sea surface and damp the *SV* oscillations; then, it should automatically disengage the hook from the *SV* and lift the hook to its home position. Conversely, a robot performing a *recovery* must deploy the hook in the proximity of the *SV*, autonomously identify, engage and lock the *SV* and lift the *SV* onto the ship while regulating *SV* oscillations. The additional requirements with respect to a lifting device are the automatic *SV* oscillation damping and the *SV* autonomous picking. To this end, a 4-cable underactuated *CDPR* (*UACDPR*) and a standard hoisting device are connected in parallel to a shared grasping device, which is the robot *EE* (Fig. 1). The rationale behind this choice is that the *UACDPR* substitutes workers and their low-power but highly dextrous job, leaving the hoisting device to perform the high-power lifting. In other words, the proposed *UACDPR* aims at enhancing the functionalities of standard hoisting devices so that they can autonomously *track* and fetch a payload. This activity will hereafter be called *tracking* and steadily *lift* it, which will be referred to as *lifting*.

The *UACDPR* is composed of 4 servo-controlled winches [20] mounted at the vertices of a square, whose center is attached to the hoist cable; both the *UACDPR* and hoisting device cables are routed by swivelling pulleys [21] from the winches to the *EE* (Fig. 1). The latter is equipped with an automated hook, which can autonomously close when impacting an eyelet on the *SV*. Cable connections on the *EE* are designed to be as close to a single point as realistic mechanical components, such as double swivel lifting rings, allow it (Fig. 2); this feature aims at reproducing an approximate spherical joint between the cable attachment points on the *EE* and the *EE*, to prevent the transmission of moments to the cables and thus limit the installed power. Such a cable robot can thus redundantly control the position of the approximated spherical joint, which is necessary for the tracking operation. In contrast, it can only damp the attitude oscillations of the *EE*, which the other operations also need. Despite the simplicity of the design with respect to other *CDPRs* used in marine environments, the system is conceptually suitable for achieving the desired goals.

3 MODEL

This section presents the overall system model used to perform custom simulations, as described in Sec 5. Section 3.1 details the geometric model of the cable-driven system and the *PV*, whereas Secs. 3.2 and 3.3 respectively present the geometric model of the *SV* and the overall system dynamics. The latters are specialized for *tracking* and *lifting* operations.

3.1 Geometric models of the Cable-driven system and the *PV*

The *PV* is modeled as a 6-*DoF* rigid body, with a frame $P_B x_B y_B z_B$ attached to its buoyancy center. x_B

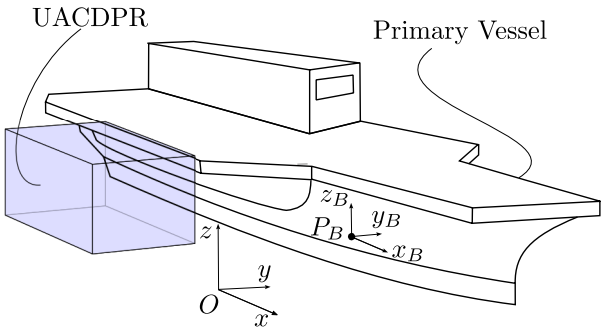

Fig. 3: Primary vessel.

axis is aligned with the *PV* propulsion direction, from stern to bow, z_B is normal to the *PV* deck and points upward and $y_B = z_B \times x_B$, where $\times$ denotes the vector product (see Fig. 3). The *PV* pose with respect to (w.r.t.) the inertial frame $Oxyz$ is $\boldsymbol{\zeta}_B = \left[\mathbf{p}_B, \boldsymbol{\theta}_B\right]^T$, where $\mathbf{p}_B$ is the position vector of P_B and $\boldsymbol{\theta}_B$ is a set of yaw ($\theta_{B,z}$), pitch ($\theta_{B,y}$) and roll ($\theta_{B,x}$) Euler angles. The rotation matrix describing the *PV* rotation w.r.t. the inertial frame is thus $\boldsymbol{R}(\boldsymbol{\theta}_B) = \boldsymbol{R}_z(\theta_{B,z})\boldsymbol{R}_y(\theta_{B,y})\boldsymbol{R}_x(\theta_{B,x})$, where $\boldsymbol{R}_z(\cdot)$, $\boldsymbol{R}_y(\cdot)$ and $\boldsymbol{R}_x(\cdot)$ are, respectively, elementary rotation matrices about z, y and x coordinate axes.

The *ALARS* installed on the *PV* can be geometrically modeled as a 5-cable *UACDPR* (Fig. 1). The pose of the 6-*DoF EE* is described by its pose $\boldsymbol{\zeta} = [\mathbf{p}^T \boldsymbol{\epsilon}^T]^T$, where $\mathbf{p}$ is the position vector of P and $\boldsymbol{\epsilon}$ is another set of yaw, pitch and roll Euler angles, in the inertial frame $Oxyz$. Each cable is considered massless and non-elastic and is guided from the winch to the *EE* by a swiveling pulley. The cable enters the pulley in point D_i, which is fixed w.r.t. the *PV*, exits from point B_i and it is attached to the *EE* in A_i. The constraint imposed by each cable on the *EE* is given by:

$$\lambda_i = \boldsymbol{\rho}_i^T \boldsymbol{\rho}_i - \left[l_i - \widehat{B_i D_i}\right]^2 = 0 \tag{1}$$

where $\boldsymbol{\rho}_i \triangleq \mathbf{a}_i - \mathbf{b}_i$, $\mathbf{a}_i$ and $\mathbf{b}_i$ are respectively the positions of A_i and B_i in the inertial frame and l_i is the cable length, comprising the rectilinear part $\|\boldsymbol{\rho}_i\|$ and the arc $\widehat{B_i D_i}$ wrapped on the pulley [18]. Differently from common *CDPRs*, the frame of the *ALARS* rigidly moves with the *PV* due to sea conditions. As a result, Eq. (1) is a system of 5 non-linear equations with 17 unknowns (5 cable lengths l_i, 6 *PV* pose variables $\boldsymbol{\zeta}_B$ and 6 *EE* pose variables $\boldsymbol{\zeta}$). However, when simulating the *ALARS*, the *PV* motion is assigned, depending on the ship type and the sea state under consideration [22]. Consequently, the position of D_i and the orientation of each swiveling axis can be computed and the system becomes geometrically equivalent to a *UACDPR*. If the pose of the *EE* is assigned, as in the inverse kinematic problem, the cable lengths can be computed through Eq. (1) [18]. On the contrary, the forward kinematic problem has infinite solutions: the problem can be solved approximately, or additional sensors can reduce the problem complexity [23].

The knowledge of the *PV* motion is also necessary when computing the differential kinematics of the robot. If the twists of the *PV* and the *EE* are, respectively, $\mathbf{v}_B = \left[\dot{\mathbf{p}}_B, \boldsymbol{\omega}_B\right]^T$ and $\mathbf{v} = \left[\dot{\mathbf{p}}, \boldsymbol{\omega}\right]^T$, the cable velocity $\dot{l}_i$ can be obtained by differentiating Eq. (1) w.r.t. time [18]:

$$\dot{\lambda}_i = \boldsymbol{\xi}_i^T \mathbf{v} - \boldsymbol{\xi}_i^{B,T} \mathbf{v}_B - \dot{l}_i = 0 \tag{2}$$

$$\boldsymbol{\xi}_i = \begin{bmatrix} \mathbf{t}_i \\ (\mathbf{a}_i - \mathbf{p}) \times \mathbf{t}_i \end{bmatrix}, \qquad \boldsymbol{\xi}_i^B = \begin{bmatrix} \mathbf{t}_i \\ (\mathbf{a}_i - \mathbf{p}_B) \times \mathbf{t}_i \end{bmatrix} \tag{3}$$

where $\mathbf{t}_i = \boldsymbol{\rho}_i / \|\boldsymbol{\rho}_i\|$ is the cable direction and $(\cdot)$ is the scalar product between vectors. The second-order differential relationship between actuation, *EE* and *PV* variables is obtained by differentiating Eq. (2) w.r.t. time:

$$\ddot{\lambda}_i = \boldsymbol{\xi}_i^T \dot{\mathbf{v}} + \dot{\boldsymbol{\xi}}_i^T \mathbf{v} - \boldsymbol{\xi}_i^{B,T} \dot{\mathbf{v}}_B - \dot{\boldsymbol{\xi}}_i^{B,T} \mathbf{v}_B - \ddot{l}_i = 0 \tag{4}$$

The explicit derivation of $\dot{\boldsymbol{\xi}}_i$ is lengthy and it is omitted for the sake of brevity, but it can be found in [18]; $\dot{\boldsymbol{\xi}}_i^B$ can be derived analogously.

3.2 *SV* geometric model

The *SV* is modeled differently depending on the activity that the *ALARS* is performing. When the *EE* is *tracking* the *SV* before engaging and locking it, the *SV* is modeled as a point mass moving in space, corresponding to the point where the *EE* should lock it. The position of this point mass is denoted as $\mathbf{p}_L$ in $Oxyz$ and its motion is assigned similarly to the *PV* depending on the vessel type and the sea state [22].

When the *EE* has locked the *SV* and *lifting* begins, the connection between the *EE* and the *SV* is modeled as a spherical joint. Depending on the physical device used for connection, different joints could be considered, but the spherical joint was deemed sufficiently accurate when the joint is of the hook-eyelet type. Thus,

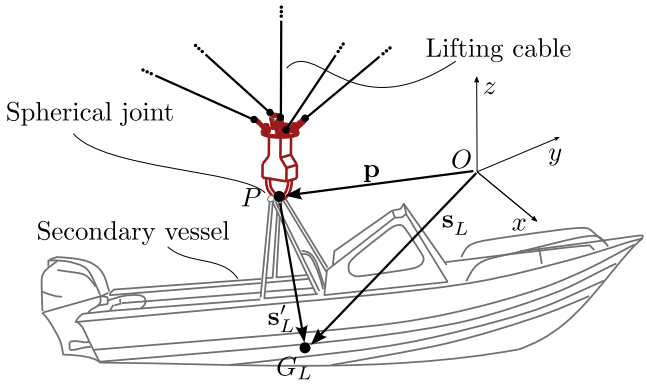

Fig. 4: Secondary vessel coupled with the end-effector of the *ALARS*.

the only additional degrees of freedom to consider for the *SV* are the rotational ones, namely an array of yaw, pitch and roll Euler angles $\boldsymbol{\theta}_L$. If we assume the center of the spherical joint to be point P and the position vector between the joint center and the *SV* center of mass to be $\mathbf{s}'_L$ in the inertial frame, the position $\mathbf{s}_L$ of the *SV* center of mass with respect to the inertial frame and its derivatives, are given by:

$$\begin{aligned} \mathbf{s}_L &= \mathbf{p} + \mathbf{s}'_L, \quad \dot{\mathbf{s}}_L = \dot{\mathbf{p}} + \boldsymbol{\omega}_L \times \mathbf{s}'_L \\ \ddot{\mathbf{s}}_L &= \ddot{\mathbf{p}} + \boldsymbol{\alpha}_L \times \mathbf{s}'_L + \boldsymbol{\omega}_L \times (\boldsymbol{\omega}_L \times \mathbf{s}'_L) \end{aligned} \tag{5}$$

with $\boldsymbol{\omega}_L$ and $\boldsymbol{\alpha}_L$ being the angular velocity and acceleration of the *SV*, respectively. Note that $\mathbf{s}'_L$ components vary as the *SV* rotates.

3.3 Dynamic models

The dynamic models presented in this section are specialized for *tracking* and *lifting* since both the system input and the mechanical models differ. When *tracking*, the central 5-th cable, namely the *lifting* or crane cable, is supposed to be slack and the dynamics of a 4-cable *UACDPR* is considered. Cable tensions are considered system inputs to control the *EE* pose behavior [24], as detailed in Sec. 4.1. During *lifting*, the 5-th cable is taut and, conforming to lifting device regulations [25], it is velocity commanded, while the remaining cables are tension controlled; additionally, the *EE-SV* assembly behaves as a double parallel-serial pendulum.

3.4 Tracking model

Under the assumption of massless and non-elastic cables, the dynamics of an *UACDPR* coincide with the one of its *EE*. The latter is a rigid body subject to cable constraints, inertial actions and external wrenches [26]:

$$\mathbf{M}\dot{\mathbf{v}} = -\boldsymbol{\Xi}^T \boldsymbol{\tau} - \mathbf{C}\mathbf{v} + \boldsymbol{\phi} \tag{6}$$

$$\mathbf{M} \triangleq \begin{bmatrix} m\mathbf{I}_{3\times3} & -m\tilde{\mathbf{s}}' \\ m\tilde{\mathbf{s}}' & \mathbf{I}_P \end{bmatrix}, \qquad \mathbf{C} \triangleq \begin{bmatrix} \mathbf{0}_{3\times3} & -m\tilde{\boldsymbol{\omega}}\tilde{\mathbf{s}}' \\ \mathbf{0}_{3\times3} & \tilde{\boldsymbol{\omega}}\mathbf{I}_P \end{bmatrix} \tag{7}$$

$$\boldsymbol{\Xi}^T = [\boldsymbol{\xi}_1, \ldots, \boldsymbol{\xi}_4], \qquad \boldsymbol{\phi} \triangleq m \begin{bmatrix} \mathbf{g} \\ \tilde{\mathbf{s}}'\mathbf{g} \end{bmatrix} \tag{8}$$

where:

m is the *EE* mass and $\mathbf{I}_P$ is the *EE* inertia matrix about its reference point P expressed in the inertial frame;
$\boldsymbol{\Xi}$ is the geometric Jacobian matrix of the system, $\boldsymbol{\tau}$ is an array containing the tensions of the four lateral cables, $\boldsymbol{\phi}$ is the external wrench due to gravity, $\mathbf{s}'$ is the *EE* center of mass position w.r.t. P in $Oxyz$, $\mathbf{g}$ is gravity acceleration
$\sim$ over a vector denotes its skew-symmetric representation and $\mathbf{I}_{3\times3}$ and $\mathbf{0}_{3\times3}$ are identity and zero matrices of order 3.

Matrix $\mathbf{M}$ is symmetric, positive-definite and invertible. Thus, $\dot{\mathbf{v}}$ can be integrated from Eq. (6) by standard solution techniques for ordinary differential equations (ODE).

3.5 Lifting model

During lifting, the *EE* dynamics of Eq. (6) is modified by:

the fifth cable constraint, since the cable is taut;
the *SV* angular dynamics.
the control method of the fifth cable: while the four lateral cables are tension-controlled, the fifth cable is velocity-controlled and l_5 motion profile needs to be considered when integrating the system dynamics.

If $\tau_5 \boldsymbol{\xi}_5$ is the constraint force exerted by the lifting cable and $\mathbf{f}$ is the force transmitted by the *SV* to the *EE* through the spherical joint, the *EE* dynamics can be rewritten as:

$$\mathbf{M}\dot{\mathbf{v}} + \mathbf{C}\mathbf{v} - \boldsymbol{\phi} + \tau_5\boldsymbol{\xi}_5 + \mathbf{A}\mathbf{f} = -\boldsymbol{\Xi}^T\boldsymbol{\tau}, \; \mathbf{A} \triangleq [\mathbf{I}_{3\times3}; \mathbf{0}_{3\times3}]^T \tag{9}$$

If m_L is the *SV* mass and $\mathbf{I}_L$ its inertia matrix about point P expressed in the inertial frame, the *SV* dynamics is given by:

$$m_L\ddot{\mathbf{s}}_L = m_L\mathbf{g} + \mathbf{f} \tag{10}$$

$$\mathbf{I}_L\boldsymbol{\alpha}_L + \tilde{\boldsymbol{\omega}}_L\mathbf{I}_L\boldsymbol{\omega}_L + m_L\tilde{\mathbf{s}}'_L\ddot{\mathbf{p}} = m_L\tilde{\mathbf{s}}'_L\mathbf{g} \tag{11}$$

Lastly, the kinematics of the fifth cable can be accounted for during integration by considering Eq. (1) (and its derivatives) alongside Eqs. (9) (*EE* dynamics) and (11) (*SV* angular dynamics). The equations to be solved are partly differential and partly algebraic, known as a differential-algebraic system of equations (DAE). In mechanical systems, DAEs are usually transformed into ODEs with so-called penalty-based relaxation methods [27]. This method avoids the exact solution of Eq. (1) (and its derivatives), by formulating a *penalized constraint* differential equation in the form:

$$\ddot{\lambda}_5 + 2\Omega\delta\dot{\lambda}_5 + \Omega^2\lambda_5 = 0 \tag{12}$$

where Ω and δ are equivalent to the natural frequency and the damping ratio of a mass-spring-damper vibrating system. Ω and δ are tunable parameters whose values must be heuristically selected as a trade-off between ODE solution accuracy, stability and computational time [28].

Finally, substituting Eq. (4) in Eq. (12) and rearranging yields:

$$\boldsymbol{\xi}_5^T\dot{\mathbf{v}} = b \tag{13}$$

$$b \triangleq \ddot{l}_5 - \dot{\boldsymbol{\xi}}_5^T\mathbf{v} - \boldsymbol{\xi}_5^{B,T}\dot{\mathbf{v}}_B - \dot{\boldsymbol{\xi}}_5^{B,T}\mathbf{v}_B - 2\Omega\delta\dot{\lambda}_5 - \Omega^2\lambda_5 \tag{14}$$

The overall lifting dynamic model is obtained by joining Eqs. (9) (*EE* dynamics), (11) (*SV* angular dynamics) and (13) (penalized constraint dynamics) and substituting Eqs. (5) and (10) in Eq. (9) to eliminate $\mathbf{f}$:

$$\mathbf{M}_L\mathbf{x} = \mathbf{c}_L + {\Xi_L}^T\boldsymbol{\tau}, \quad {\Xi_L}^T = \begin{bmatrix} -\Xi^T \\ \mathbf{0}_{4\times4} \end{bmatrix}, \quad \mathbf{x} = \begin{bmatrix} \ddot{\mathbf{p}} \\ \boldsymbol{\alpha} \\ \boldsymbol{\alpha}_L \\ \tau_5 \end{bmatrix} \tag{15}$$

$$\mathbf{c}_L = \begin{bmatrix} m\tilde{\boldsymbol{\omega}}\tilde{\mathbf{s}}'\boldsymbol{\omega} + m_L\tilde{\boldsymbol{\omega}}_L\tilde{\mathbf{s}}'_L\boldsymbol{\omega}_L + (m+m_L)\mathbf{g} \\ -\tilde{\boldsymbol{\omega}}\mathbf{I}_P\boldsymbol{\omega} + m\tilde{\mathbf{s}}'\mathbf{g} \\ -\tilde{\boldsymbol{\omega}}_L\mathbf{I}_L\boldsymbol{\omega}_L + m_L\tilde{\mathbf{s}}'_L\mathbf{g} \\ b \end{bmatrix} \tag{16}$$

$$\mathbf{M}_L = \begin{bmatrix} (m+m_L)\mathbf{I}_{3\times3} & -m\tilde{\mathbf{s}}' & -m_L\tilde{\mathbf{s}}'_L & \mathbf{t}_5 \\ m\tilde{\mathbf{s}}' & \mathbf{I}_P & \mathbf{0}_{3\times3} & -\tilde{\mathbf{t}}_5(\mathbf{a}_5-\mathbf{p}) \\ m_L\tilde{\mathbf{s}}'_L & \mathbf{0}_{3\times3} & \mathbf{I}_L & \mathbf{0}_{3\times1} \\ \mathbf{t}_5^T & (\mathbf{a}_5-\mathbf{p})^T\tilde{\mathbf{t}}_5 & \mathbf{0}_{1\times3} & 0 \end{bmatrix} \tag{17}$$

Matrix $\mathbf{M}_L$ is also symmetric and positive-definite, thus invertible. $\mathbf{x}$ can be calculated by solving the linear system in Eq. (15) and the differential portion of the vector, namely $[\ddot{\mathbf{p}}^T\boldsymbol{\alpha}^T\boldsymbol{\alpha}_L^T]^T$, integrated with standard ODE solution techniques.

4 CONTROL

The controllers presented in this section are differently tailored for *tracking* and *lifting*, since *ALARS* objective during these tasks is fundamentally different. When *tracking*, the *EE* reference position $\mathbf{p}$ needs to follow the *SV*, which is modeled as a point mass whose position is $\mathbf{p}_L$ (see Sec. 3.2). The tensions of the four lateral cables are regulated to minimize the distance between the *SV* and the *EE*, namely $\mathbf{d} = \mathbf{p} - \mathbf{p}_L$. During *lifting*, the 5-th cable is velocity commanded, namely $\dot{l}_5$ follows a prescribed motion law, conforming to lifting regulations [25]. The tension of the four lateral cables is regulated to damp any *EE* and *SV* motion other than the vertical translation.

4.1 Tracking controller

Tracking controllers for *UACDPR* are very limitedly studied and only a few applications tailored to specific architectures are reported in the literature (see [29] for an example on 2-cable 3-*DoF* planar *UACDPRs* and [30] for an application to 2-cable 3-*DoF* point-mass *UACDPRs*). Thus, a controller suitable for the robot architecture at hand and the *tracking* task is here developed.

There are two main problems to be solved in controlling an *UACDPR*. The first one consists in reliably estimating the pose of the *EE* in order to increase the robustness and stability of the controller [31]: indeed, due to underactuation, the *EE* pose cannot be inferred through standard direct kinematics. The second problem regards selecting which subset of the *UACDPR* pose variables are to be controlled, how to control them and how to manage the uncontrolled internal dynamics of the *EE* [30].

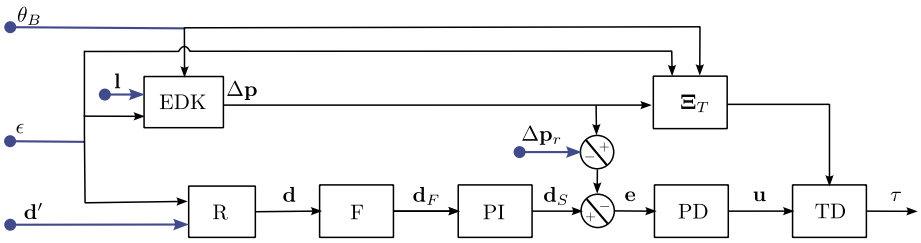

Fig. 5: Tracking control diagram

In this paper, the first problem is solved by employing extra sensors on the *PV* and the *EE*. This choice is mainly an engineering one: extra sensors provide redundancy, can aid diagnostics and may ultimately be used for several control purposes (such as *SV* detection). Two Attitude and Heading Reference Systems (*AHRS*) are supposed to be installed on both the robot frame (thus on the *PV*) and on the *EE*: thanks to these sensors, $\boldsymbol{\theta}_B$ and $\boldsymbol{\epsilon}$ can be measured. Then, at any time instant, l_i ($i = 1,\dots,4$) is also measured and $\Delta\mathbf{p} = \mathbf{p} - \mathbf{p}_B$ is determined by minimizing the system of non-linear equations provided by Eq. (1) (this strategy is also referred to as Extended Direct Kinematics, *EDK* [23, 31]).

The choice of the controlled variables is straightforward in this application, since we wish to minimize the distance between the *SV* and the *EE* position. Since four cables are available, a redundant control of the *EE* position, instead of regulating an additional orientation variable, is chosen. Depending on the shape of the locking interface between *SV* and *EE*, a large orientation difference between them can be tolerated when engaging, if the controlled position is accurate and the *EE* internal dynamics stable [32]. On the other hand, cables need to be kept taut to operate and the redundant control action can be used toward this end. Ultimately, cable tensions can be regulated according to a Proportional-Derivative (*PD*) controller with gravity compensation [33], which results in the following Tension Distribution (*TD*):

$$\boldsymbol{\tau} = \text{sat}(m\Xi_T^{+}(\boldsymbol{u}+\mathbf{g}) + \mu\Xi_T^{\perp}) \tag{18}$$

where Ξ_T^{+} and $\Xi_T^{\perp}$ are the Moore-Penrose pseudo-inverse and nullspace of matrix $\Xi_T^T = [\mathbf{t}_1,\dots,\mathbf{t}_4]$, which is the translational portion of the Jacobian in Eq. (8) and $\mathbf{u}$ is the output of the *PD* controller. At any time instant, Ξ_T^T can be calculated after $\Delta\mathbf{p} = \mathbf{p} - \mathbf{p}_B$ is estimated as detailed above. In contrast, μ is a scalar parameter that can be computed to minimize the tension difference among the cables with a linear program [34]. sat$(\cdot)$ is a saturation function and if its inputs exceed lower or upper positive bounds, namely τ_m and τ_M, the outputs are set to τ_m or τ_M: cables are thus always kept taut at the expense of the control objectives.

The rest of the controller structure can be observed in Fig. 5, where the blue dots represent measured variables on the system. The displacement of the *SV* from the *EE* is acquired by a camera mounted on the *EE* and is measured in the *EE* frame as $\mathbf{d}'$. $\mathbf{d}'$ is rotated in the inertial frame as $\mathbf{d}$, then it is lowpass filtered as $\mathbf{d}_F$, which it ultimately is processed by a *PI* regulator as $\mathbf{d}_S$. Due to technological limitations, camera information is acquired at a lower frequency (20 Hz max) than the computation of cable tension set-points (1 kHz); the low pass filter and the *PI* controller aim at smoothening the camera signal from noise, providing the subsequent control block with a more gradually changing signal than a step and compensating steady-state errors thanks to integral action. Lastly, the output $\mathbf{d}_S$ of the PI controller is fed into a cascade control loop with the *PD* controller. This technique improves the stability and linear characteristics of the resulting feedback linearized system, which is ultimately realized through the Tension Distribution (TD) block. Computing the TD as in Eq. (18) performs a sort of feedback linearization of the *UACDPR* dynamics with respect to the position variables, which is in general not robust with respect to modeling errors and disturbances.

The *PD* control loop uses a modified feedback of the *EE* position which is computed as $\Delta\mathbf{p} - \Delta\mathbf{p}_r$, where $\Delta\mathbf{p}_r$ is the value of $\Delta\mathbf{p}$ when the tracking controller is activated. This way, the tracking loop is referred to the *EE* instantaneous position when the *tracking* starts. Should $\Delta\mathbf{p}$ be used without the $\Delta\mathbf{p}_r$ correction, a larger error would result at the beginning of tracking, possibly resulting in a large overshoot due to the proportional action of the controller, which is ultimately not allowed on a real system (the *EE* would crash on the *SV*). Thanks to the correction, the error that inputs the controller is initially limited to $\mathbf{d}_s$, resulting in a gentler start of the tracking procedure and no overshoot, even if the pro-

portional gain is high or not optimally tuned.

4.2 Lifting controller

The lifting controller objective is peculiar. After the *EE* grasps the *SV*, lifting is initiated by controlling the length of the central lifting cable. If the *EE*-*SV* assembly is not centered w.r.t. to the robot frame, which is the usual case due to *PV* oscillations, the assembly dangerously swings. The controller aims at damping the *EE* and *SV* swinging, while also mitigating *EE* and *SV* angular free motion. To this end, lateral cables *lifting* Tension Distribution is chosen as:

$$\boldsymbol{\tau} = \text{sat}(\tau_0 \mathbf{I}_{4\times 4} + \gamma \dot{\mathbf{l}}) = \text{sat}(\tau_0 \mathbf{I}_{4\times 4} + \gamma \boldsymbol{\Xi} \mathbf{v}) \tag{19}$$

where γ is a positive non-zero constant, $\dot{\mathbf{l}} \triangleq \boldsymbol{\Xi}\mathbf{v}$ is the array of lateral cable velocities and τ_0 is a desired value for all cable tensions at static equilibrium. Swinging and angular motion damping are thus achieved by limiting cable velocities and keeping a tension τ_0. Please note that the sign of γ leads to a dissipative effect due to our conventions: cable velocities are positive when cables are fed into the workspace, or, in other words, the winch is unwound. When the *EE* pulls on the cables, attempting to unwind them, cable tensions are then increased with respect to τ_0 according to Eq. (19). Dynamically speaking, when Eq. (19) is substituted in Eq. (15), a damping term is added to the unforced dynamics of the system [30]. Depending on the value of τ_0 and γ, lateral cables will be more or less quick at damping. For high values of τ_0 and γ, the *ALARS* is very effective at damping *EE* motion, but very high power and cable tensions are required in the cables, which is ultimately undesirable. If γ is generally low, damping would be poor, whereas if τ_0 is too low, the controller will always be saturating (and ultimately not damping *EE* motion). Depending on the required performance and desired power consumption, parameters can be optimized.

5 SIMULATION CAMPAIGN

A comprehensive simulation campaign is conducted to investigate operation feasibility, determine system performance and ultimately obtain winch design parameters, such as maximum cable velocity, tension and power. The *ALARS* is supposed to handle different types of *SV*, which, depending on their type, are characterized by different sea-induced motion to track and mass and inertia to lift and stabilize. The geometrical parameters used for the simulated systems can be found in Tab. 1, where $\mathbf{d}_i$ is the position of D_i in the ship frame, $\mathbf{a}'_i$ the distance of A_i from P in the *EE* frame, r_i the radius of each pulley and $\mathbf{x}_i$,$\mathbf{y}_i$ and $\mathbf{z}_i$ are unit vectors defining the reference orientation of the swiveling pulleys [18]: such parameters are sufficient for computing Eq. (1), its derivatives and all the geometry-related terms used in the dynamic models and controllers. As far the *EE* is concerned, the vertical distance of the center of mass from P is 0.2 m, the mass is $m = 93.6$ Kg and the inertia matrix components in the *EE* frame are $I_{P,xx} = 4.75$ Kgm^2 , $I_{P,yy} = 4.75$ Kgm^2 and $I_{P,zz} = 0.6$ Kgm^2. Minimum and maximum cable tensions are set to $\tau_m = 100$ N and $\tau_M = 10000$ N.

Table 1: Geometrical parameters of the *ALARS*

i	1	2	3	4	5
$\mathbf{d}_i$ [m]	$\begin{bmatrix}-0.5\\-10.1\\7\end{bmatrix}$	$\begin{bmatrix}-0.5\\-13.1\\7\end{bmatrix}$	$\begin{bmatrix}-3.5\\-13.1\\7\end{bmatrix}$	$\begin{bmatrix}-3.5\\-10.1\\7\end{bmatrix}$	$\begin{bmatrix}-2\\-11.6\\7\end{bmatrix}$
$\mathbf{a}'_i$ [m]	$\begin{bmatrix}0.05\\0.05\\0.5\end{bmatrix}$	$\begin{bmatrix}0.05\\-0.05\\0.5\end{bmatrix}$	$\begin{bmatrix}-0.05\\-0.05\\0.5\end{bmatrix}$	$\begin{bmatrix}-0.05\\0.05\\0.5\end{bmatrix}$	$\begin{bmatrix}0\\0\\0.5\end{bmatrix}$
r_i [m]	0.075	0.075	0.075	0.075	0.150
$\mathbf{x}_i$	-**j**	−**j**	**j**	**j**	**j**
$\mathbf{y}_i$	-**k**	-**k**	-**k**	-**k**	-**k**
$\mathbf{z}_i$	**i**	**i**	-**i**	-**i**	-**i**

5.1 Tracking simulations

The primary objective of the *tracking* simulation is to verify if the *UACDPR* is able to track a *SV* with the proposed controller. To this end, simulations are run while recursively tuning controller parameters to adjust performances. Secondarily, given a tuned system, we seek to understand which class of *SV* and thus which kind of motion, the *ALARS* is able to successfully track.

Simulations are performed by integrating the *EE* motion from Eq. (6), where cable tensions are computed by Eq. (18). The necessary input parameters to perform the simulations are: (i) the *EE* initial pose and twist, so that a well-defined ODE can be established from Eq. (6), (ii) the *PV* and *SV* motion profiles, where the former is needed to compute the *ALARS* model variables, whereas the latter is needed for computing $\mathbf{d}'$ and consequently the controller output and (iii) the tracking controller parameters.

Not all the *PV* pose $\boldsymbol{\zeta}_B$ coordinates are variable during simulations. Ship velocity along x_B (surge) and y_B (sway) and its angular velocity about z_B (yaw) are supposed to be zero, while velocity along z_B (heave), pitch and roll are sinusoidal [22]. In our simulations, only pitch and roll motions are considered since they

Table 2: *SV* motion parameters

	RHIB - 7 m	RHIB - 9.35 m	RHIB - 11 m
A_{roll}	7 °	7 °	7 °
A_{pitch}	2 °	2 °	2 °
f_{roll}	0.1818 Hz	0.1724 Hz	0.1587 Hz
f_{pitch}	0.2857 Hz	0.25 Hz	0.25 Hz
$\mathbf{s}'_L$ [m]	$\begin{bmatrix} 0 \\ 0 \\ -1.1 \end{bmatrix}$	$\begin{bmatrix} 0 \\ 0 \\ -1.5 \end{bmatrix}$	$\begin{bmatrix} 0 \\ 0 \\ -1.7 \end{bmatrix}$
m	4000 Kg	7500 Kg	12000 Kg
$I_{L,xx}$	14500 Kgm^2	27200 Kgm^2	43500 Kgm^2
$I_{L,yy}$	33100 Kgm^2	62100 Kgm^2	99300 Kgm^2
$I_{L,zz}$	26500 Kgm^2	49700 Kgm^2	79500 Kgm^2

are deemed to be the most critical for task feasibility: they may effectively bring the *SV* vessel outside the *PV* reachable workspace. The *SV* position $\mathbf{p}_L$ is also obtained by considering the *SV* pitch and roll oscillations about its center of mass. Finally, all the angular oscillations have the form $\upsilon = A_\upsilon \cos(2\pi f_\upsilon t + \varphi_\upsilon)$, where A_υ, f_υ and φ_υ are oscillation amplitude, frequency and phase, respectively.

To achieve the primary objective of the tracking simulations and verify feasibility while iteratively and manually updating controller parameters, *PV* pitch and roll amplitude and frequency are set, according to [22] and a sea-state of four, to $A_{\theta_{B,x}} = 7$ °, $A_{\theta_{B,y}} = 1$ °, $f_{\theta_{B,x}} = 0.075$ Hz, $f_{\theta_{B,y}} = 0.2$ Hz. Pitch and roll phases are discretely varied from 0 to 2π in each simulation, since *PV* pitch and roll phase influence the *EE* initial pose before *tracking* starts and consequently the total tracking time. The *SV* parameters are assumed to be those of a 7 m RHIB (Rigid Hull Inflatable Boat, see tab. 2), which is a frequent type of *SV*. The position of the *SV* center of mass is centered 0 m below the *ALARS* frame when the pitch and roll of the latter are zero; *SV* roll and pitch oscillation phases are set to zeros, as they only negligibly impact the simulation results. The *EE* initial position is always 3.1 m below the *ALARS* frame and its initial orientation is the same as the *PV*; the initial twist is set to zero, assuming that a controller similar to the lifting one can be used to bring the *EE* in the desired initial position and keep it steady. The tuned parameters are the following: the cut-off frequency of the filter is 20 Hz, the proportional and integral coefficients of the first PI controller are 0.4 and 3.2 s^{-1} respectively and the proportional and derivative coefficients of the second PD controller are 12.5 and 4.5 s respectively. An example of simulation results, where the *PV* phases were each set to $\pi/4$, is shown in Fig. 6. From Fig. 6a we may see how the *EE* tracks the SV with some delay, due to the controller structure. Still, it should be considered that the *PV* frame oscillates with an amplitude of approximately 1 m in the horizontal direction and of 1.5 m in the vertical direction and the *SV* $\mathbf{p}_L$ with an amplitude of approximately 0.2 m in the horizontal direction (vertical motion is negligible). *EE* orientation is stable around an amplitude of 7° for roll (Fig. 6d), 1.5° for pitch (Fig. 6e) and is negligible for yaw (Fig. 6f). Maximum cable speed is 1.5 m/s (Fig. 6g), maximum power 650 W (Fig. 6i) and cable tensions don't exceed 610 N: please note that cable tensions are subject to frequent saturation at τ_m (Fig. 6h) and this limits the controller performance. All in all, there are several time intervals when the distance $\|\mathbf{d}\|$ between the *EE* and the *SV* approaches zero and locking is achievable (see Fig. 6c). In general, our simulations showed that when the *PV* pitch and roll phases are different from the ones reported in Figs. 6 and 7, the overall tracking performances change negligibly.

To achieve the secondary objective of the tracking simulations, controller parameters are kept constant while the *SV* ship type is varied according to tab. 2; consequently *SV* pitch and roll amplitude, frequency and phase also vary. Figure 7 shows that if *SV* vessel has larger and faster motion, horizontal tracking is poorer in absolute terms (Fig. 7a), but $\mathbf{p}_L$ motion amplitude is twice as large. Nonetheless, locking could also be achievable in several time intervals (see Fig. 7c). *EE* orientation still oscillates stably (Figs. 7d, 7e and 7f) and cable velocities, tensions and power are not affected by the larger and faster motion of the *SV* (Figs. 7g, 7h, 7i): the proposed tracking controller is very stable due to the proposed structure, but a strategy for its performance adjustment should be sought in the future.

5.2 Lifting simulations

While tracking simulations were primarily concerned with feasibility from a control perspective, the primary objective of the *lifting* simulation is to determine the specifications on the *ALARS* winches necessary to damp *EE* and *SV* oscillations during operations. In fact, *lifting* is the most demanding activity in terms of power and cable tensions, since the *SV* may weigh up to 100 times the *EE*; even though the hoisting cable lifts most of the weight, lateral cables still need to compensate for *EE* and *SV* inertial actions, which are non-negligible even at low speed and accelerations.

Simulations are performed by integrating the lifting dynamic model in Eq. (15), where cable tensions are computed by Eq. (19). The necessary input parameters to perform the simulations are (i) the *EE* initial pose and

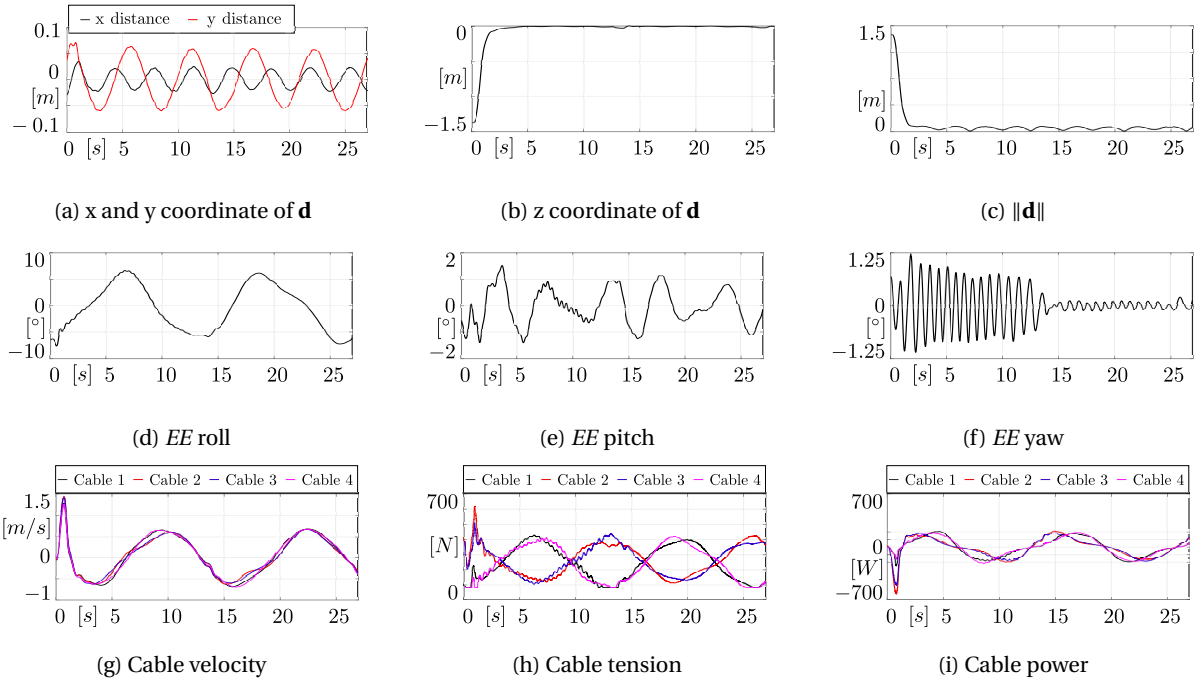

(a) x and y coordinate of **d**

(b) z coordinate of **d**

(c) $\|\mathbf{d}\|$

(d) *EE* roll

(e) *EE* pitch

(f) *EE* yaw

(g) Cable velocity

(h) Cable tension

(i) Cable power

Fig. 6: Tracking simulation results for the 7 m RHIB.

twist and the *SV* initial angular configuration and velocity, (ii) the *PV* and lifting cable motion profiles and (iii) the lifting controller parameters.

PV motion parameters are selected the same as in *tracking* simulations, that is, motion frequency and amplitudes are constant, whereas phases are varied. The reason behind this choice is to determine if, for an assigned *PV* motion profile, the *ALARS* is able to successfully lift its payload regardless of when the operation is initiated. The lifting cable follows a standard trapezoidal velocity profile [17], with 0.15 m/s^2 acceleration and decelerations applied for 1 s, a nominal lifting speed of 0.15 m/s and a final cable length of 1.7 m corresponding to the *EE* home position. *SV* angular configuration and angular velocity are set to zero, *EE* initial position is always 5 m below the *ALARS* frame and 1 m offset in the global y direction, its initial orientation is the same as the *PV* and the initial twist is set to zero. The *SV* and *EE* initial conditions are compatible with the cables maintaining a low tension after tracking and before lifting, when the *SV* is still in the water: this way, the cables would naturally stabilize the *EE-SV* assembly motion, which is thus considered negligible (a more in-depth analysis will be considered in the future). The controller parameters are tuned to $\tau_0 = 10000$ N and $\gamma = 20000$ Ns/m. Minimum and maximum cable tensions are set to $\tau_m = 100$ N and $\tau_M = 10000$ N: $\tau_0 = \tau_M$ effectively provides best damping performance.

Figure 8 shows an example of simulation results. Figure 8a clearly shows that the *EE* position $\mathbf{p}$ asymptotically reaches the *ALARS* frame center $\mathbf{p}_B$ during lifting. Figures 8d, 8e and 8f also show the controller effectiveness in damping *EE* oscillations. The very high-frequency yaw oscillations are due to model simplifications, such as neglecting friction: in practice, they will be quickly damped by frictional effects, which were disregarded in this study. The very simple controller presented in Sec. 4.2 also allows damping the *SV* roll oscillations, as can be seen in Fig. 8g, but it is ineffective in damping pitch and yaw oscillations (Figs. 8h and 8i). On the other hand, the *SV* pitch is naturally small and stable, whereas the *SV* yaw is not oscillatory and could be limited by designing a suitable *EE-SV* interface able to eliminate such a freedom: both these aspects are not

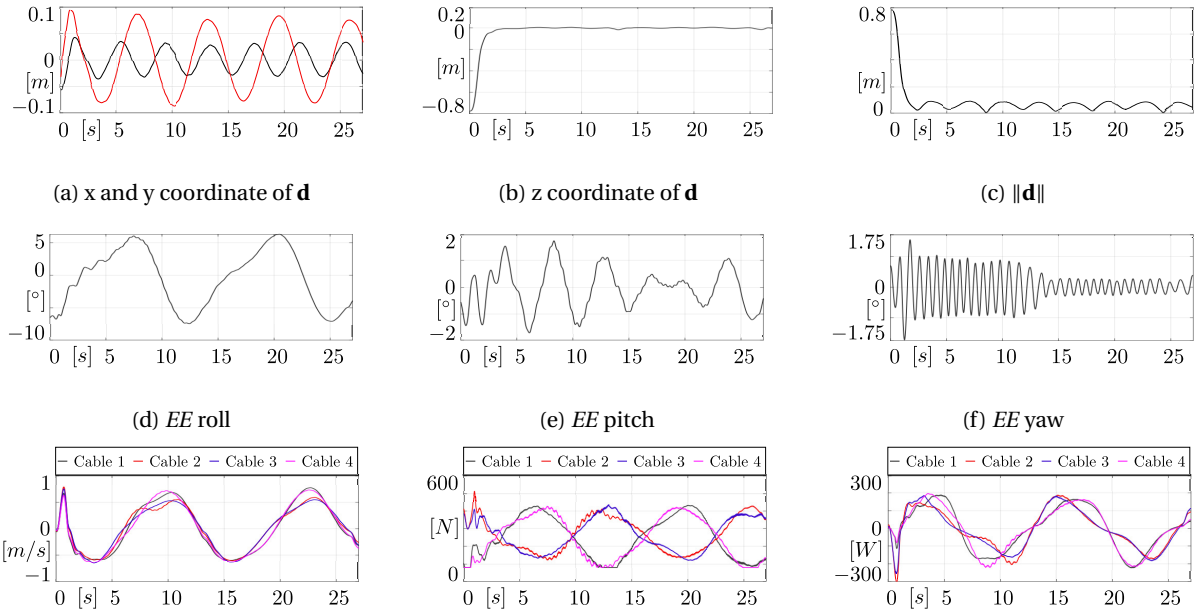

(a) x and y coordinate of **d**

(b) z coordinate of **d**

(c) $\|\mathbf{d}\|$

(d) *EE* roll

(e) *EE* pitch

(f) *EE* yaw

(g) Cable velocity

(h) Cable tension

(i) Cable power

Fig. 7: Tracking simulation results for the 11 m RHIB.

a problem for the lifting operations, as the fundamental objective here is to bring the *EE*-*SV* assembly in the center of the *ALARS* workspace, regardless of where the *SV* has been grasped, so as to avoid the *SV* crashing with the *PV*. During lifting, both minimum and maximum tension saturation occur (Fig. 8k), but such a phenomenon does not produce appreciable performance degradation. The maximum required power is shown to be 2200 W. During our simulation campaign, we noticed that the *PV* roll and its derivative when *lifting* is started have a strong impact on achieving a stable lift. Generally, it is better to start lifting when the *PV* is closer to the sea and moving away from it. In this way, the sea-induced *PV* motion helps in lifting, thus reducing the power required to the cables. On the contrary, if lifting is started when the *PV* is moving towards the sea, the *SV* could be unpredictably moved in and out of the water, thus degrading the overall task performance.

6 EXPERIMENTAL DEMONSTRATION

A demonstrator of the system is developed by adapting an *UACDPR* prototype available at IRMA-L@B [35], and installed at L3Harris facilities in Bologna. A 2 m × 2 m frame is hanged 5 m above ground thanks to a gantry crane (Fig. 9). The robot geometric parameters can be found in Tab. 3. An experimental automatic hook, which was developed in a separate study by the Laval University Robotics Laboratory [36], is used as the robot *EE*. Such a hook is software commanded for opening and closing but is also equipped with a mechanical trigger that allows automatic closure when a payload is hit. An Intel RealSense D435i stereo camera was mounted on the *EE* to track the distance between the *EE* and a *mockup payload*. The latter consists of a ring to be grasped, 20 kg of steel plates, and a red ball operating as a reference to be tracked by the camera (see the payload in Fig. 9). The payload is located on a shuttle that may perform linear motions at 45° w.r.t. the horizontal plane. The payload shuttle is commanded

Table 3: Geometrical parameters of the prototype

i	1	2	3	4	5
$\mathbf{d}_i$ [m]	$\begin{bmatrix}-1\\-1\\5\end{bmatrix}$	$\begin{bmatrix}-1\\1\\5\end{bmatrix}$	$\begin{bmatrix}1\\1\\5\end{bmatrix}$	$\begin{bmatrix}1\\-1\\5\end{bmatrix}$	$\begin{bmatrix}0\\0\\5\end{bmatrix}$
$\mathbf{a}'_i$ [m]	$\begin{bmatrix}0.05\\0.05\\0\end{bmatrix}$	$\begin{bmatrix}0.05\\-0.05\\0\end{bmatrix}$	$\begin{bmatrix}-0.05\\-0.05\\0\end{bmatrix}$	$\begin{bmatrix}-0.05\\0.05\\0\end{bmatrix}$	$\begin{bmatrix}0\\0\\0\end{bmatrix}$
r_i [m]	0.05	0.05	0.05	0.05	0.05
$\mathbf{x}_i$	**-j**	**−j**	**j**	**j**	**j**
$\mathbf{y}_i$	**-k**	**-k**	**-k**	**-k**	**-k**
$\mathbf{z}_i$	**i**	**i**	**-i**	**-i**	**-i**

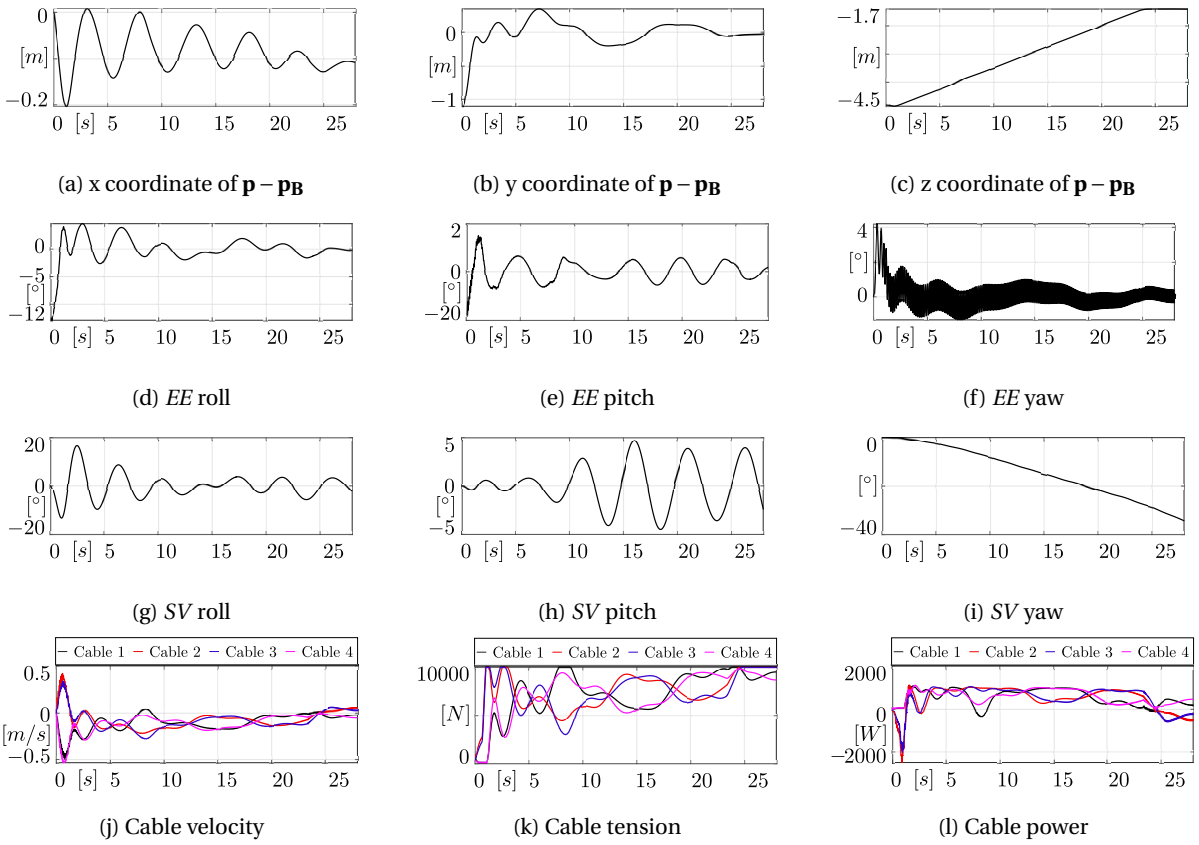

(a) x coordinate of $\mathbf{p} - \mathbf{p_B}$ (b) y coordinate of $\mathbf{p} - \mathbf{p_B}$ (c) z coordinate of $\mathbf{p} - \mathbf{p_B}$

(d) *EE* roll (e) *EE* pitch (f) *EE* yaw

(g) *SV* roll (h) *SV* pitch (i) *SV* yaw

(j) Cable velocity (k) Cable tension (l) Cable power

Fig. 8: Lifting simulation results for the 7 m RHIB.

to perform a sinusoidal motion with 0.25 Hz frequency and 0.3 m amplitude, according to the expected *SV* motion parameters reported in Tab. 2.

A *Recovery* operation is performed, but only the tracking portion of the operation was deemed safe to perform with nominal capabilities (i.e. *EE* speed, payload oscillation amplitude and frequency) in a laboratory environment with a scaled prototype (payload mass could not weigh several tons, since it could have harmed people and equipment). The phases leading to the autonomous tracking and picking of an object are here reported to show the capabilities of the system. For the adapted prototype at hand, the controller parameters necessary for the lifting and tracking operations reported in Sec. 4 were tuned by trial and error for optimal results, starting from the simulation results reported in Sec. 5, since several real-world disturbances were present during the experiments (camera lag, sensor noise, imperfect calibration).

From a homing configuration, the *EE* is *deployed* to a configuration suitable for the *EE*-mounted camera to start detecting the payload, by using only the lifting controller: the central cable is unwound to the prescribed length of 2.5 m, while the lateral cables stabilize the *EE* ($t = 0 \ldots 25$ s in Fig. 10). Then, lifting-controller outputs and tracking-controller outputs are averaged for 10 s so as to smoothly transition from the lifting controller to the tracking controller (light blue area in Fig. 10). At 35 s the actual trajectory tracking starts and it can be clearly seen in Fig. 10 that the *EE* is able to rapidly minimize the tracking error and maintain it bounded until the experiment is stopped at $t = 102$ s. For picking reasons, the z-coordinate fed to the controller is offset by 0.5 m, so that the payload can be picked by *dropping* the *EE* on it, thus hitting the *EE* mechanical trigger, simply removing the offset when the 2-norm of the tracking error is stably below a threshold, which was set to 5 cm.

The video attached to the paper [37] shows the experimental set-up and implementation of the *recovery* operation, where the deployment, tracking, and dropping phases can be appreciated. The red marker on

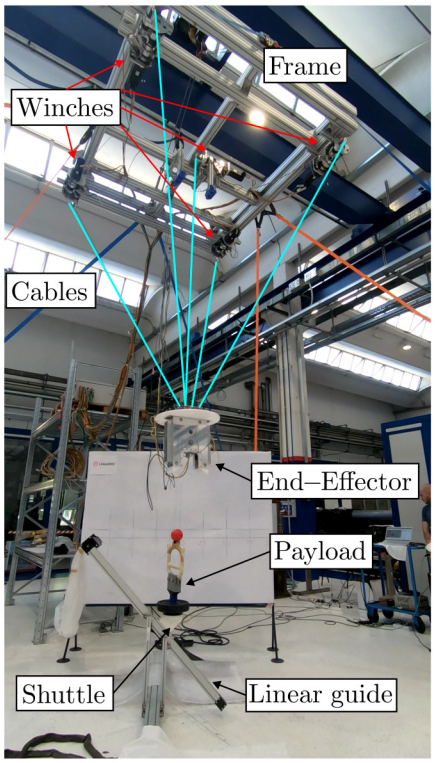

Fig. 9: Experimental Layout

top of the mockup payload was removed since it would have mechanically interfered with the dropping operation. Accordingly, tracking set points were virtually generated, as the camera could not track a distinctive feature on the *EE*. To stress our controller, the sinusoidal frequency of the payload was set to 0.33 Hz. Nonetheless, it can be seen that tracking is satisfactorily achieved, and the payload is correctly picked.

7 CONCLUSIONS

This paper presented the conceptual design and control of an automatic launch and recovery system based on the coupling of an underactuated cable-driven parallel robot with a hoisting device. The simulation campaign showed that the system is theoretically effective for achieving the goals of launching and retrieving vessels from and to a mothership; additionally, simulations allowed to determine the size of winch components for production and hinted at potential problems to be solved by hardware, such as (i) design the *EE-SV* locking interface so that is able to accommodate for 10 cm of horizontal error and 7° degrees of angular misalignment and which is able to constrain the *SV* yaw motion. Experiments on a scaled prototype showed promising results in terms of the effectiveness of the proposed system, and allowed us to highlight the most critical aspect to be tackled during industrialization, namely the performance of the tracking controller due to real-world disturbances. Currently, a full-scale prototype is being developed by L3Harris for laboratory and in-field testing.

REFERENCES

[1] Angelini, M., Ida', E. I., Bertin, D., Carricato, M., Mantovani, E., Bazzi, D., and Orassi, V., 2023, "An underactuated cable-driven parallel robot for marine automated launch and recovery operations," In Proceedings of the ASME IDETC-CIE 2023, Boston, MA, USA, August 20-23.

[2] Abdolshah, S., Zanotto, D., Rosati, G., and Agrawal, S., 2017, "Performance evaluation of a new design of cable-suspended camera system," In IEEE International Conference on Robotics and Automation, pp. 3728–3733.

[3] Bruckmann, T., Lalo, W., Nguyen, K., and Salah, B., 2012, "Development of a storage retrieval machine for high racks using a wire robot," In ASME International Design Engineering Technical Conferences & Computers and Information in Engineering Conference, pp. 771–780.

[4] Bruckmann, T., and Boumann, R., 2021, "Simulation and optimization of automated masonry construction using cable robots," *Advanced Engineering Informatics*, **50**(101388), pp. 1–14.

[5] Izard, J.-B., Gouttefarde, M., Baradat, C., Culla, D., and Sallé, D., 2013, "Integration of a parallel cable-driven robot on an existing building façade," In *Cable-Driven Parallel Robots*, T. Bruckmann and A. Pott, eds. Springer, Berlin, Heidelberg, pp. 149–164.

[6] Idà, E., Marian, D., and Carricato, M., 2020, "A deployable cable-driven parallel robot with large rotational capabilities for laser-scanning applications," *IEEE Robotics and Automation Letters*, **5(3)**, pp. 4140–4147.

[7] Hu, Y., Tao, L., and Lv, W., 2014, "Anti-pendulation analysis of parallel wave compensation systems," *Institution of Mechanical Engineers, Part M: Journal of Engineering for the Maritime Environment*, **230(1)**, pp. 177–186.

[8] Gouttefarde, M., Lamaury, J., Reichert, C., and Bruckmann, T., 2015, "A versatile tension distribution algorithm for n -dof parallel robots driven by

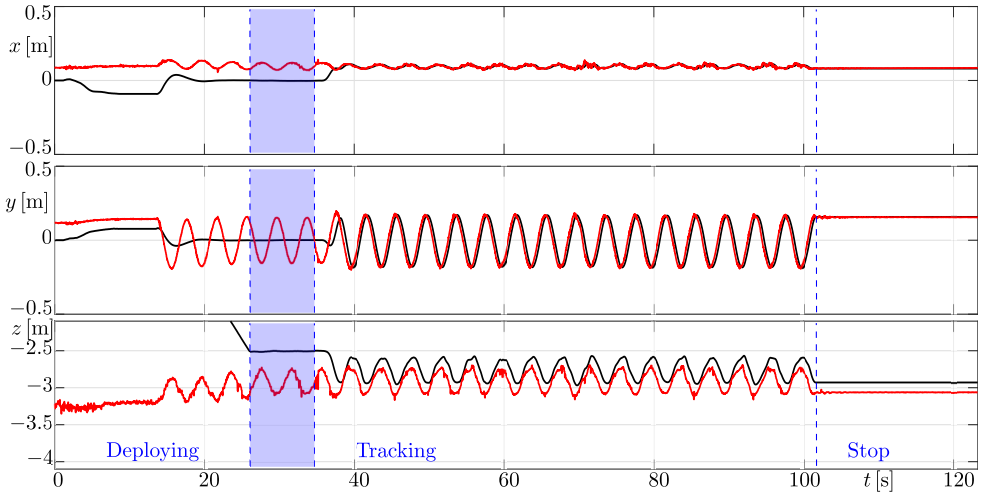

Fig. 10: Recovery experimental results: the *EE* position reconstructed by the Extended Direct Kinematics is in black, whereas the payload position, as reconstructed with the camera system, is in red. Blue lines delimit the operation phases, and the light blue area highlights where tracking and lifting controllers are averaged.

$n+2$ cables," *IEEE Transactions on Robotics*, **31(6)**, pp. 1444–1457.

[9] Kery, S., Hughes, G., May, E., Kjolseth, P., Pang, M., Thomas, W., Treakle, T., and Liut, D., 2005, "Achieving high container through-put rates, between vessels in high seas (a vision of hicass)," In MTS/IEEE OCEANS conference, pp. 454 – 459.

[10] Lv, W., Tao, L., and Hu, Y., 2017, "On the real-time calculation of the forward kinematics of a suspended cable-driven parallel mechanism with 6-degree-of-freedom wave compensation," *Advances in Mechanical Engineering*, **9(6)**, pp. 1–17.

[11] Lv, W., Tao, L., and Ji, Z., 2017, "Design and control of cable-drive parallel robot with 6-dof active wave compensation," In International Conference on Control, Automation and Robotics, pp. 129–133.

[12] Tong, Y., and He, J., 2018, "Dynamics and force regulation of fully constrained cable-driven parallel mechanism as a marine salvage device," In IEEE International Conference of Intelligent Robotic and Control Engineering, pp. 60–63.

[13] Horoub, M. M., Hassan, M., and Hawwa, M. A., 2018, "Workspace analysis of a gough-stewart type cable marine platform subjected to harmonic water waves," *Mechanism and Machine Theory*, **120**, pp. 314 – 325.

[14] Horoub, M., Hassan, M., and Hawwa, M., 2019, "A floating cable-driven robotic manipulator in a marine environment," In *Advances in Mechanism and Machine Science*, T. Uhl, ed. Springer, Cham, pp. 2893–2906.

[15] Bertin, D., 2022, Guided lifting system EP3988440A1,.

[16] Idà, E., and Carricato, M., 2021, "A new performance index for underactuated cable-driven parallel robots," In *Cable-Driven Parallel Robots*, M. Gouttefarde, T. Bruckmann, and A. Pott, eds. Springer, Cham, pp. 24–36.

[17] Idà, E., Briot, S., and Carricato, M., 2021, "Robust trajectory planning of under-actuated cable-driven parallel robot with 3 cables," In *Advances in Robot Kinematics*, J. Lenarčič and B. Siciliano, eds. Springer, Cham, pp. 65–72.

[18] Idà, E., Briot, S., and Carricato, M., 2021, "Natural oscillations of underactuated cable-driven parallel robots," *IEEE Access*, **9**, pp. 71660–71672.

[19] Mottola, G., Gosselin, C., and Carricato, M., 2018, "Dynamically-feasible elliptical trajectories for fully constrained 3-dof cable-suspended parallel robots," In *Cable-Driven Parallel Robots*, C. Gosselin, P. Cardou, T. Bruckmann, and A. Pott, eds. Springer, Cham, pp. 219–230.

[20] Idà, E., and Mattioni, V., 2022, "Cable-driven parallel robot actuators: State of the art and novel servo-winch concept," *Actuators*, **11(10)**(290), pp. 1–13.

[21] Lucarini, A., and Idá, E., 2022, "Kinematic modeling and design of a sensorized cable-routing system for cable-driven parallel robots," In *Advances in Italian Mechanism Science*, V. Niola, A. Gasparetto, G. Quaglia, and G. Carbone, eds. Springer, Cham, pp. 77–85.

[22] United States Department of Defense, 1986,

Interface standard for shipboard system section 301a ship motion and attitude (metric). https://publishers.standardstech.com/content/military-dod-usdod_dod-std-1399-301 Accessed: 27 February 2023.

[23] Gabaldo, S., Idà, E., and Carricato, M., 2022, "Sensitivity of the direct kinematics of underactuated cable-driven parallel robots to redundant sensor-measurement errors," In *Advances in Robot Kinematics 2022*, O. Altuzarra and A. Kecskeméthy, eds. Springer, Cham, pp. 131–138.

[24] Santos, J. C., Gouttefarde, M., and Chemori, A., 2022, "A nonlinear model predictive control for the position tracking of cable-driven parallel robots," *IEEE Transactions on Robotics,* **38(4)**, pp. 2597–2616.

[25] Det Norske Veritas, 2021, Launching appliances for work boats and tender boats https://global.ihs.com/doc_detail.cfm?&document_name=DNV-ST-0498 Accessed: 27 February 2023.

[26] Idà, E., Briot, S., and Carricato, M., 2022, "Identification of the inertial parameters of underactuated cable-driven parallel robots," *Mechanism and Machine Theory,* **167**(104504), pp. 1–14.

[27] Bettega, J., Piva, G., Richiedei, D., and Trevisani, A., 2023, "Model predictive control for path tracking in cable driven parallel robots with flexible cables: collocated vs. noncollocated control," *Multibody System Dynamics*, pp. 1–35 Advance online publication, https://doi.org/10.1007/s11044-023-09881-0.

[28] Flores, P., Machado, M., Seabra, E., and Tavares da Silva, M., 2010, "A Parametric Study on the Baumgarte Stabilization Method for Forward Dynamics of Constrained Multibody Systems," *Journal of Computational and Nonlinear Dynamics,* **6(1)**(011019), 10, pp. 1–9.

[29] Harandi, M. R. J., and Taghirad, H. D., 2021, "Adaptive interconnection and damping assignment passivity-based control for an underactuated cable-driven robot," *International Journal of Adaptive Control and Signal Processing,* **35(12)**, pp. 2487–2498.

[30] Harandi, M. R. J., Khalilpour, S. A., and Taghirad, H. D., 2022, "Adaptive energy shaping control of a 3-dof underactuated cable-driven parallel robot," *IEEE Transactions on Industrial Informatics*, pp. 1–9 Advance online publication, https://doi.org/10.1109/TII.2022.3211980.

[31] Gabaldo, S., Idà, E., and Carricato, M., 2023, "Pose-estimation methods for planar underactuated cable-driven parallel robots," In Cable-Driven Parallel Robots, S. Caro, A. Pott, and T. Bruckmann, eds., Springer, pp. 3–15.

[32] Harandi, M. R. J., Damirchi, H., Khalilpour, S. A., and Taghirad, H. D., 2019, "Point-to-point motion control of an underactuated planar cable driven robot," In 27th Iranian Conference on Electrical Engineering, pp. 979–984.

[33] Kelly, R., 1997, "PD control with desired gravity compensation of robotic manipulators: A review," *The International Journal of Robotics Research,* **16(5)**, pp. 660–672.

[34] Oh, S.-R., and Agrawal, S., 2005, "Cable suspended planar robots with redundant cables: controllers with positive tensions," *IEEE Transactions on Robotics,* **21(3)**, pp. 457–465.

[35] IRMAL@B, 2023, Irmal@b research cable-driven parallel robots https://irmalab.org/research/cable-driven-robots/ Accessed: 15 July 2023.

[36] Laboratoire de robotique, 2023, Laval university robotics laboratory website https://robot.gmc.ulaval.ca/en/home/ Accessed: 15 July 2023.

[37] Ida', E., 2023, Recovery demonstration video https://youtu.be/uhcU0XngIXU Accessed: 17 April 2024.